Advanced Alumina Dissolution Modelling

V. Bojarevics and M. Dupuis

Abstract

Alumina feeding requires optimization for the feed amount, timing, and point feeder locations. The alumina raft formation and dispersion are the essential stages leading to the particles of various sizes travel with the bath flow along anodes in the central channel, in the bath volume beneath the anodes, and gradually dissolving. The raft motion and particles are traced accounting for their inertia, drag in the turbulent flow, the dome-shaped anode bottom shape. Large-scale MHD-driven circulation in the cell is modelled using specific inputs corresponding to real commercial cells of various types. The feed material forming rafts and particles is added periodically, moves with the flow, and gradually dissolves depending on the local turbulence and instantaneous concentration in a location. The newly developed modelling technique is applied to illustrate possible optimization of the feeder locations, the variable mass, and feeding time intervals for possible adjustments suitable for commercial cells.

Keywords

Aluminium electrolysis cell • Alumina dissolution • Particle tracking • Magneto hydrodynamics • Turbulent mixing

V. Bojarevics (✉)
School of Computing and Mathematics, University of Greenwich, 30 Park Row, London, 10 9LS, UK
e-mail: v.bojarevics@gre.ac.uk

M. Dupuis
Genisim Inc., 3111 Alger St., Jonquiere, Québec, G7S 2M9, Canada
e-mail: marc.dupuis@genisim.com

Introduction

Alumina feeding is a critical aspect of the operation of a modern aluminium reduction cell. Historically, this was done very inefficiently; the side crust was broken at two and a half to three-hour intervals, and then a huge amount of alumina was dumped over the open crust. This led to the formation of a lot of sludge. Anode effects were frequent, acting as a clean-up of the cell at a regular interval. Figure 1 presents the measured temperature and alumina concentration evolution of a side broken Soderberg cell for 24 h. We can see that 4 anode effects occurred in that cell during the day which was a very typical situation.

In the early 1960s, Alcoa introduced a major innovation to the process, the point breaker feeder (PBF), which together with the introduction of the continuous tracking computer control logic by Pechiney in the 1970s [2] led to the drastic reduction of the anode effect frequency and duration, and a significant increase of the current efficiency.

Unfortunately, with the recent increase of the cell sizes, increase of the anode sizes, and the corresponding reduction of bath volume, combined with the increase of the PBF load, a continuous contribution to PFC emissions started to be reported first in China [3] and then elsewhere [4, 5].
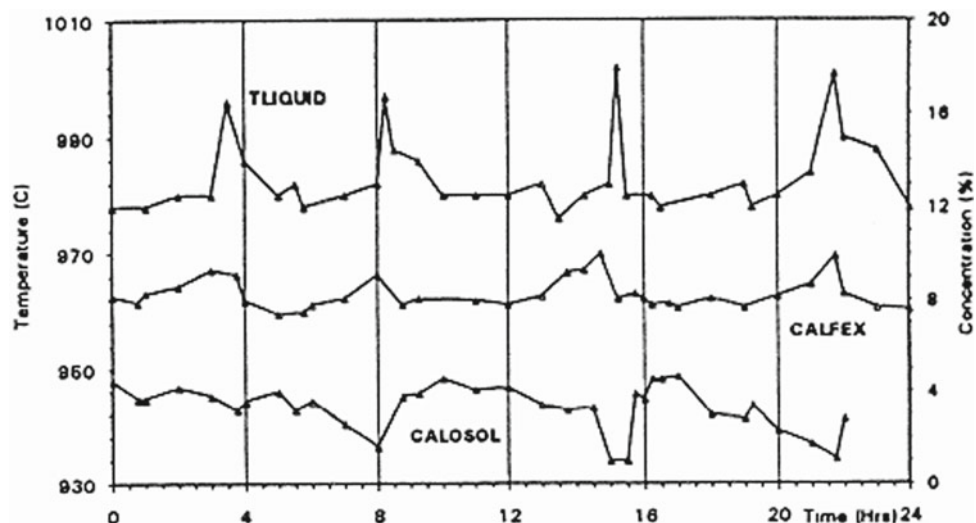
This motivated the R&D effort to better understand and develop models of the complex alumina dissolution process. In particular, raft formation, displacement, and dispersion have been extensively studied in recent years [6–8]. The most probable physical mechanism indicates that the bulk of the alumina feed forms first a raft of particulate material which can travel along the central channel. When the frozen bath shell remelts, the raft starts to release the feed alumina particles in a process analogous to a snowfall. This was observed in a laboratory using actual bath and secondary alumina feed; see Fig. 2. The same process was replicated in a physical model to illustrate the phenomena; see Fig. 3.

The mathematical model development is on-going and proceeds in steps. The initial models were alumina

Fig. 1 Temperature, excess AlF$_3$, and dissolved alumina concentration evolution in a Soderberg cell over a period of 24 h, Fig. 2 of [1]

dispersion models only, assuming the alumina was fed as already dissolved [9, 10]. Then some actual alumina dissolution models were developed where alumina solid particles are fed; those particles then dispersed and dissolved [11, 12]. Running those 3D models in transient mode requires a lot of CPU time. These models rely on the previously calculated 3D MHD flow, and sometimes also on the 3D bubble-driven flow, which requires a lot of CPU time to get a solution. For this reason, usage of these models remains very limited due to the prohibitive CPU requirements.

Furthermore, these 3D alumina dissolution models neglect the physics of the raft formation, displacement, and eventual dismantling away from the feeding position. Recently, at least one model was developed to specifically reproduce what happens when a given mass of cold solid alumina particles is added to the bath [13]. Figure 4 displays the predicted initial formation of a raft which is composed of frozen bath particles containing a shipment of dry alumina particles remaining at an incoming density to ensure the floatation of the raft. The computational time steps of such a model are in ms, so it takes significant CPU resources to solve less than 1 s history of raft formation. For this reason, it will be extremely challenging to extend the simulation

duration to reach the point where the bath starts to remelt, and the alumina particles are finally released in the bulk of the bath.

The present work is a part of modelling development effort taking advantage of the experience gained developing the very efficient shallow water MHD cell stability model and attempts to develop an equally efficient alumina dissolution model [14, 15]. More precisely, this paper presents the first attempt to incorporate the physics involving the raft presence, displacement, and dissolution in a full cell alumina feeding model. This attempt is an ongoing project; it is an incremental step in the development of an accurate and efficient alumina dissolution model.

The Theory Coupling Concentration Field and Raft, Particle Motion

The list of publications devoted to the alumina feeding problem is rather extensive, showing various approaches; see [16–22] in addition to those already covered in the Introduction. Practical usability of the complex mathematical modelling setups and the need for expensive computer
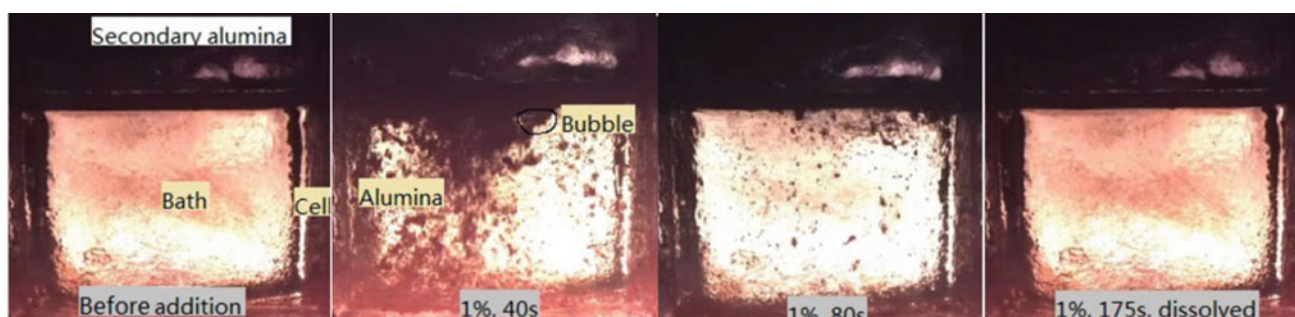

Fig. 2 Steps in the dissolution process of actual secondary alumina, from Fig. 3 of [8]

resources preclude universal acceptance of the models. In this paper, we continue the efforts to develop the software extension module to treat the alumina feeding and dissolution [14, 15], to be used as an extension of the specialised aluminium cell modelling package MHD-VALDIS [23, 24]. The modelling of the complex time-dependent feeding problem includes the full commercial cell setup, starting with the cell geometry and the surrounding bus-bar network. This permits solving the electric current distribution and the resulting magnetic fields, including the full non-linear magnetic effects of the ferromagnetic parts of the cell. The resulting 3-dimensional electromagnetic force distribution in the fluid layers is projected to an extended shallow-layer fluid dynamic problem, which is solved accounting for fully time-dependent model with the free interface wave and the depth-averaged turbulent flow [24]. The model for an MHD stable case leads to a quasi-stationary velocity field $\mathbf{v}$ in the bath layer and the turbulent effective viscosity v_e, from which the turbulent diffusivity α_e can be deduced to further apply it in the modified concentration C equation to govern the dissolved alumina transport in the bath layer:

$$\partial_t C + \mathbf{v} \cdot \nabla C = \nabla \cdot (\alpha_e \nabla C) + S - P. \tag{1}$$

The concentration $C(x, y, t)$ is treated as the depth-averaged quantity due to the small depth of the electrolyte (compared to the horizontal extent). The turbulence model permits to deduce the average velocity and the pulsating velocity part (random walk model), which are summed up within the local velocity $\mathbf{v}(x, y, t)$. The source term S in Eq. (1) provides the coupling between the C distribution of the dissolved alumina and the moving particles of various sizes. As indicated in the Introduction, the particles initially form 'rafts' of baked feed alumina material, possibly of different bulk density and of a large size. The rafts are free to move and are subject to similar forces as the small particles, however, the empirical dispersion rate is significantly different to account for the different physics involved in the dispersion process. Therefore, the source term S can be formally represented in a similar mathematical form as that for the small particle dispersion and dissolution to be obtained from the separate Lagrangian particle tracking solution at each given time moment over the full extent of the electrolyte layer:

$$S = k_2 (C_{sat} - C) \frac{A}{dV} N_{sc}, \tag{2}$$

$k_2 = 1.0 \cdot 10^{-6}$ m/s is the empirical dissolution rate constant for the small particles (e.g., from [25]) and $k_2 = 5.0 \cdot 10^{-4}$ m/s is the adjusted value for an empirically obtained raft dispersion rate (can be input by user of the software). $C_{sat} = 164.6 (kg/m^3)(\approx 8\%)$ is the saturation level of the alumina in the cryolite melt. $A(x, y, t)$ is the total sum of the surface area of all particles in the local discretised element of volume dV, and the number N_{sc} is the scaling factor to represent the correlation from the total number of particles used in the numerical simulation ($\sim$ 5000 or more in some tests) and the actual mass of the alumina being fed to the liquid bath. The alumina concentration loss term $P(x, y, t)$ is determined by the electrochemical metal reduction from the dissolved alumina:

$$P = 1.93 k_e j / h_{el} \tag{3}$$

$k_e = 9.33 \cdot 10^{-8}$ [kg/(A · s)] is the electrochemical equivalent for the aluminium metal, $j(x, y, t)$ (A/m^2) is the electric current density, h_{el} is the electrolyte depth, and the coefficient 1.93 relates the amount of alumina used to produce the aluminium metal.

The effective diffusivity $\alpha_e(x, y, t)$ in (1) is defined as the sum of laminar α and turbulent diffusivity α_T:

$$\alpha_e = \alpha + \alpha_T = \alpha + S_{ct} v_T, \qquad v_e(x, y, t) = v + v_T(k, \omega). \tag{4}$$

The simplest model for turbulent Schmidt number S_{ct} is the Reynolds analogy, which means $S_{ct} = 1$. The v_T distribution is obtained by solving the time-dependent k-ω two-equation model [26, 27]. The ω variable is related to the frequency of vorticity fluctuations, and the k variable is the turbulence kinetic energy. The depth averaging in the shallow layer approximation adds the new terms in the model [24] permitting to account for shallow layer damping and the additional turbulence generation due to the bubble flow.

The dynamic update of the concentration source term requires finding the total surface area of all particles in the local element $A(x, y, t)$. This can be obtained from the dynamic Lagrangian particle tracking model. The positions $\mathbf{R}(x, y, z, t)$ of individual particles and rafts can be determined by following their paths in the liquid according to the variable force $\mathbf{F}(x, y, z, t)$ acting on each particle at a given time moment [28, 29]:

$$\partial_t \mathbf{R} = \mathbf{u}_p, \quad m_p \partial_t \mathbf{u}_p = \mathbf{F}, \tag{5}$$

where $\mathbf{u}_p$ is the actual particle velocity and m_p is the mass. The force $\mathbf{F}$ can be decomposed into the fluid drag force $\mathbf{F}_d$, the buoyancy force $\mathbf{F}_g$, and the effective electromagnetic force $\mathbf{F}_e$; see [14] for the full representation of these components. Note that the buoyancy force on the particles floating under the anodes in the gas bubble-filled layer and on the rafts in channels is projected along the 'dome'-shaped top of the electrolyte layer, Fig. 6a. The electromagnetic force acts in the surrounding fluid, which leads to an
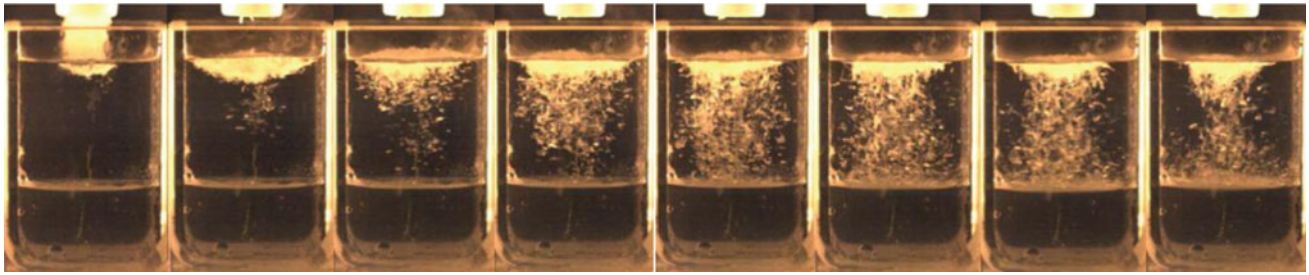
Fig. 3 Steps of the alumina dissolution process in a physical model, from Fig. 124 of [7]
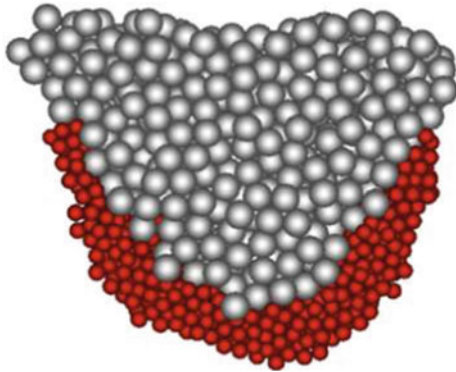

Fig. 4 Model of the raft formation, from Fig. 5 of [13]

additional pressure redistribution on the surface of the particle, giving an additional total force on the particle [30]. The drag expression for a particle needs some modification due to the acceleration or deceleration in the turbulent flow according to the memory term (Basset force) and the added mass force.

The flow in the electrolyte is turbulent ($Re \sim 10^3$–10^4), which requires a modification due to the stochastic part of

fluid velocity in accordance with the resolved turbulent kinetic energy k and the local eddy lifetime. The use of the k-ω turbulence model in the code facilitates obtaining these quantities, which are locally interpolated to the particle position at each time step. The numerical integration of Eq. (5) is done for each individual particle of various properties, including the rafts. The time-dependent forces **F** are updated in the numerical modelling at each time step $dt = 0.025$ s (or 0.0125 s for convergence tests).

Various Model Inputs and Results

Initially, the program MHD-VALDIS runs for a prescribed time interval to obtain the turbulent flow velocity distribution, the EM fields, and the bath/metal interface shape (affecting the anode bottom profile). The obtained physical fields are stored in a dedicated file for repeated use with the alumina mixing test runs, thus saving considerably the time for repeated runs of the mixing modelling for a specified commercial cell represented in detail using the program MHD-VALDIS inputs.

The generic 500 kA cell [24, 31] will be used as an example to demonstrate the modelling results. The velocity
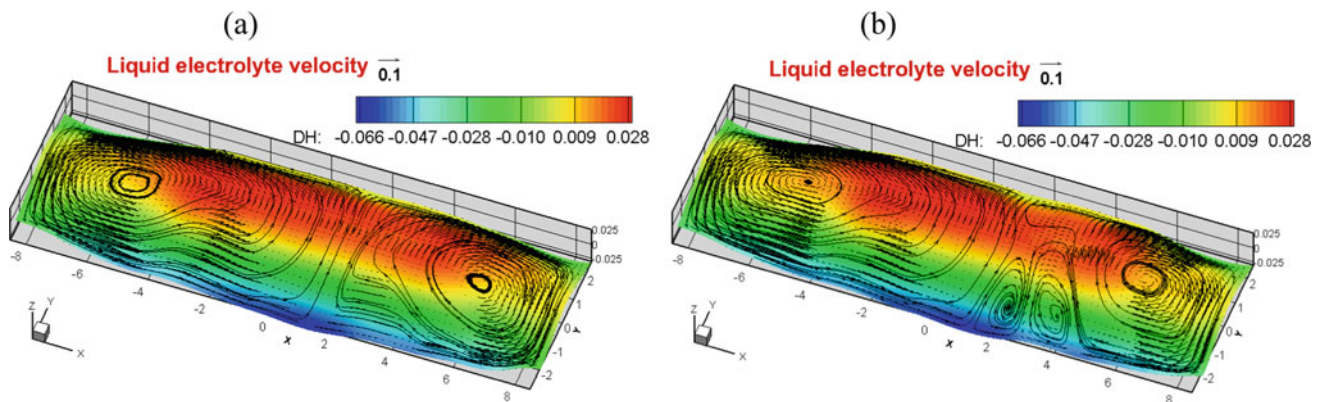

Fig. 5 **a** The velocity field in the bath and deformed quasi-stationary interface deviation dH (m) between the liquid metal and the electrolyte in the cell. **b** The velocity **v**(m/s) and the interface in the perturbed cell
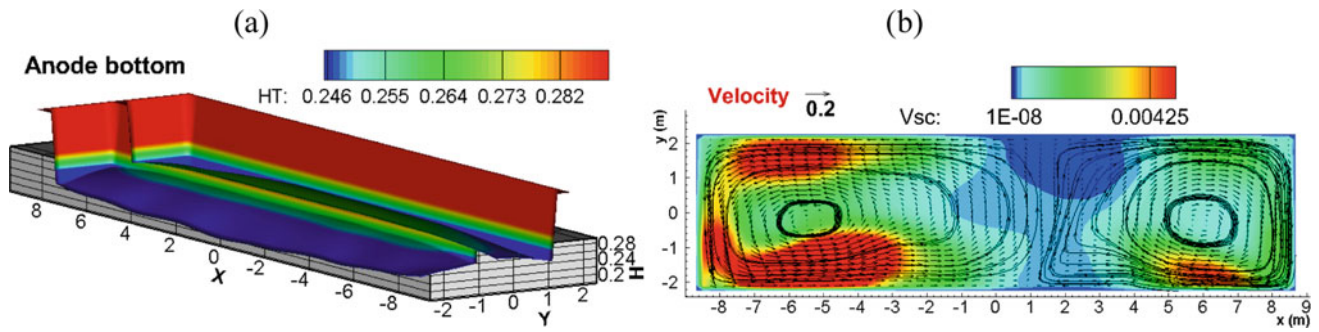
Fig. 6 **a** The position of anode bottom HT (m) from the bottom of cell cavity after the equilibrium burnout is achieved to comply with the constant ACD for the quasi-stationary interface of the liquid metal. **b** The velocity field in the liquid electrolyte and distribution of the effective turbulent viscosity (m^2/s)

field for a regular and a perturbed cell (for instance, due to an anode change disruption) is presented in Fig. 5, also showing the dome-shaped nature of the electrolyte layer beneath the similarly shaped anode blocks, Fig. 6a. The effective turbulent viscosity distribution is shown in Fig. 6b to demonstrate the highly non-uniform distribution of this essential feature for the alumina dissolution efficiency.

The feeding simulation starts after the total time of the cell MHD simulation reaches a quasi-stationary stage at the time given in the file DATA. The alumina feeding parameters can be prescribed in the text file 'Feed.txt', an example of which is presented in Table 1. In this case, the feeder locations given in Table 1 correspond to a typical choice

used in aluminium industry. The feeder positions are shown as black circles in the central channel, Fig. 7. According to the settings in the input file 'Feed.txt', the feeders are activated at intervals of 120 s when each of them supplies 2.17 kg of alumina (computed to compensate exactly the metal production according to (3)). At each cycle, the rafts of a given size and density are created at each feeder of a given fraction of the full mass introduced, the rest being assumed to reach the bath in the particulate form of the given particle size distribution; see Table 1.

The mixing solution proceeds by staring at a given initial uniform concentration (2% in this case). The particles and rafts are moving according to Eq. (5) and the concentration

Table 1 Feeding model input

```
   INPUT       | Alumina feeding model inputs: EXPLANATIONS and COMMENTS
===============|========================================================================
   3600.       |mixing time interval in (s)
      1        |EM force pressure effects: 1 means "yes", 0 - "no"
      1        |electrolyte channel & dome shape effects: 1 means "yes", 0 - "no"
      2.       |initial alumina concentration, %
   2.e3        |alumina particle density kg/m**3
  50.e-6       |1 - initial particle size in (m)
  75.e-6       |2 - initial particle size in (m)
 100.e-6       |3 - initial particle size in (m)
   1.e-6       | empirical dissolution coefficient [m/s] Haverkamp & Welch 1998
   1.5e3       | alumina particle raft density kg/m**3
   2.e-2       | alumina raft size, m  (effective spherical diameter)
   5.e-4       | raft empirical dispersion coefficient (m/s)
   0.8         | fraction of total feed mass in rafts
   120.        | feeding time interval in (s)
  -6.71        |1) feeder x-position in (m) [in cell coordinates]
   0.0         |1) feeder y-position in (m) [in cell coordinates]
   2.17        |1) feed mass in (kg)
  -3.37        |2) feeder x-position in (m) [in cell coordinates]
   0.0         |2) feeder y-position in (m) [in cell coordinates]
   2.17        |2) feed mass in (kg)
   0.01        |3) feeder x-position in (m) [in cell coordinates]
   0.0         |3) feeder y-position in (m) [in cell coordinates]
   2.17        |3) feed mass in (kg)
   3.37        |4) feeder x-position in (m) [in cell coordinates]
   0.0         |4) feeder y-position in (m) [in cell coordinates]
   2.17        |4) feed mass in (kg)
   6.71        |5) feeder x-position in (m) [in cell coordinates]
   0.0         |5) feeder y-position in (m) [in cell coordinates]
   2.17        |5) feed mass in (kg)
```
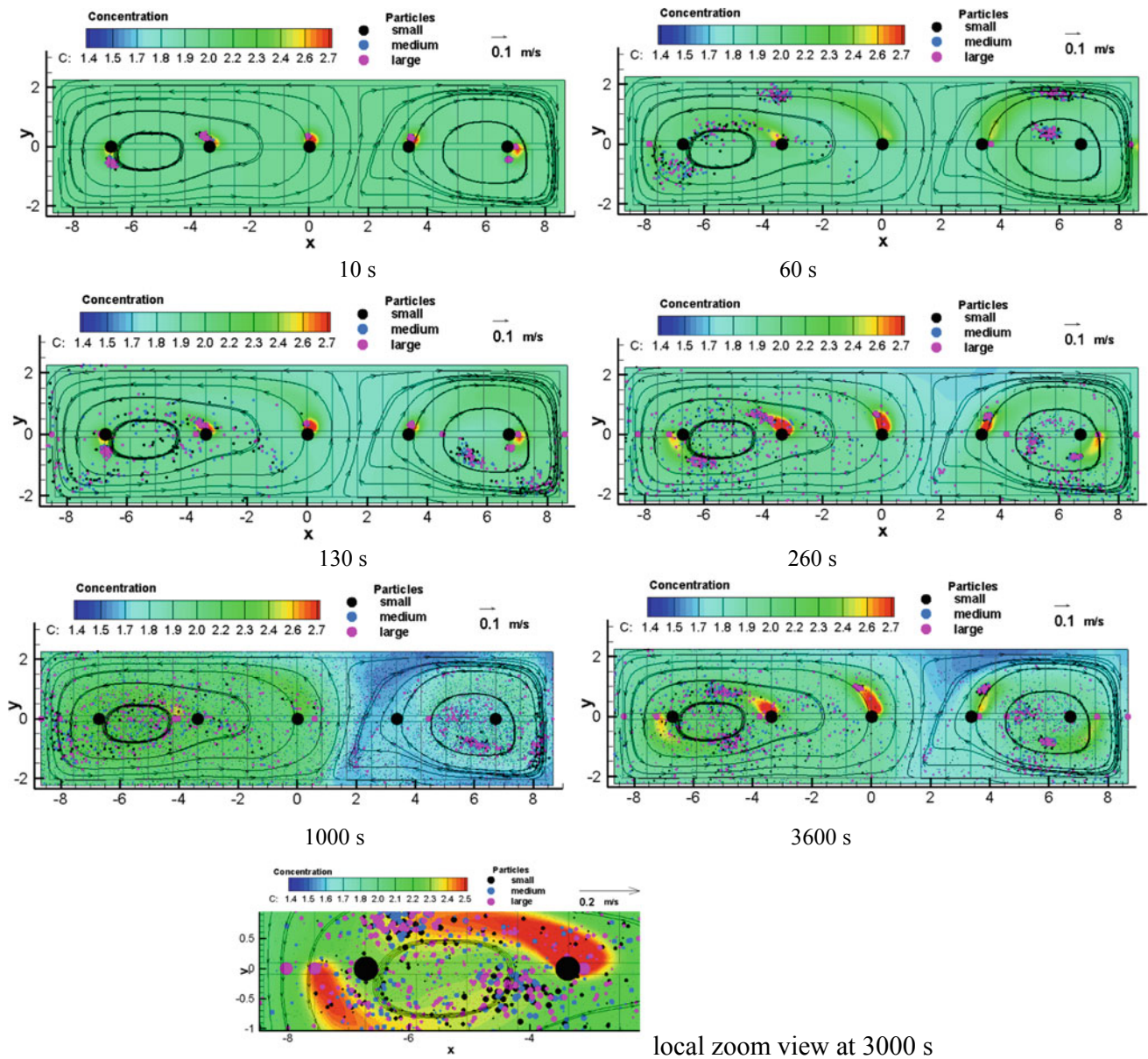
Fig. 7 The snapshots of the rafts and particles, concentration of the alumina, and the velocity streamlines for a normal feeder position choice and equal feed amount of 2.17 kg (each) at selected time moments

is updated at each time step by solving (1)–(3). At each time step, the particle and the raft lose a certain amount of volume by dissolving/dispersing, giving an updated reduced size and surface area. Due to the higher dispersion rate, the rafts disperse until they reach the size of the largest particle, then the particle behaves like a normal one. The numerical process and the result are illustrated in Fig. 7 giving some snapshots of the raft and particle positions, sizes, and the resulting concentration evolution. At the same time, the concentration is constantly reduced according to the metal production term (3). After 10 s of the initial mixing, only clouds of particles are visible, and the rafts are hidden

beneath the feeder surfaces (black dots). At the 60 s stage, the rafts are visible as they move away from the feeders overcoming the inertia along the central channel away from the feeders; the particles are being transported and dispersed (due to turbulence) by the flow, reduced in size (dissolving), and the solution concentration starts to grow locally at the largest particle and raft positions. At 130 s, the second feeding cycle is already active for 10 s, adding a new batch of particles and rafts. At 260 s, the third cycle is active, and some rafts are acting as a significant source of the alumina concentration growth, which indicates the noticeable difference from the solution without rafts. At 1000 s, we can see

Table 2 The output summary generated by the program:

```
***    Summary at end time, s            3600.00
initial bath alumina mass, kg             129.24
total added alumina,        kg            325.50
Alumina spent to produce metal, kg        324.80
Dissolved alumina,          kg            127.22
alumina left in particles, kg               5.83
average concentration,      kg/m**3        40.85
average concentration,      %               1.97
feeding estimate error,     %              -0.68
```

an advanced mixing stage after several feeding cycles and the raft redistribution and gradual disappearance according to the given dispersion rates. The concentration starts to show a highly non-uniform distribution due to the mixing and the turbulence dominance at the left side of the cell (Fig. 6b).

After following the feeding and mixing process for 1 h (3600 s) of the physical time, we can see the established pattern of the concentration loss at the right side of the cell and growth at the left side. The average concentration, however, is nearly ideally close to the initial 2% level as shown in the final simulation summary in Table 2. The alumina added (325.5 kg) and spent (324.8 kg) are almost in equal amount by mass, the dissolved total (127.22 kg) left in the bath is nearly the same as the initial (129.24 kg), and some alumina is left in particles and rafts at this stage (5.83 kg). The final balance indicates an error or relative solution accuracy by the mass disbalance as (0.0068 in relative units). This solution is of reasonable accuracy for the estimates of the technological needs. However, the distribution of the concentration gives some concern due to the raised value at the left side and the reduced one at the right

side of the cell. The numerical solution of the 1-h mixing process took about 18 min of computer time (Dell XPS 15 laptop), which permits in principle to use this in real time as a technology assistance tool.

Figure 8a demonstrates the effect of rafts on the average concentration development during the 1 h feeding sequence. Each feeding cycle (120 s) is showing an initial growth, then a drop in the concentration of alumina. The solution without rafts demonstrates a more uniform distribution close to the initial one and a balance of about 2%. The presence of rafts reduces slightly the average concentration by moving the dispersed material from the central channel at variable locations, nevertheless remaining reasonably close to the equilibrium. If the feed material is supplied at a reduced amount, say at 90% by effectively setting the feed mass per feeder at 1.953 kg and C_{in} = 2.5%, the resulting average concentration drops dramatically during the 1 h period (Fig. 8b). Similarly, by raising the feed amount at 110% (2.387 kg), C_{in} = 1.8%, the alumina concentration starts rising in the cell as indicated by solution results in Fig. 8b.

The results presented in Fig. 7 indicate that the standard choice of the feeder positions is far from the optimum,
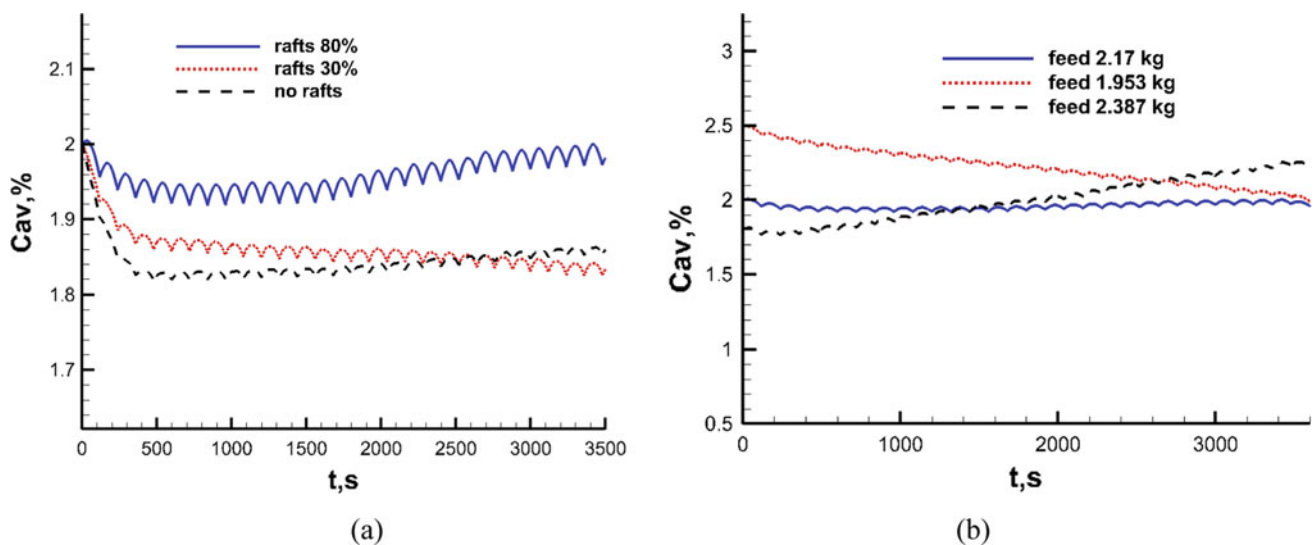

Fig. 8 **a** The effect of rafts or no rafts on the average concentration during the 1 h feeding. **b** The response when dropping or rising the feed amount
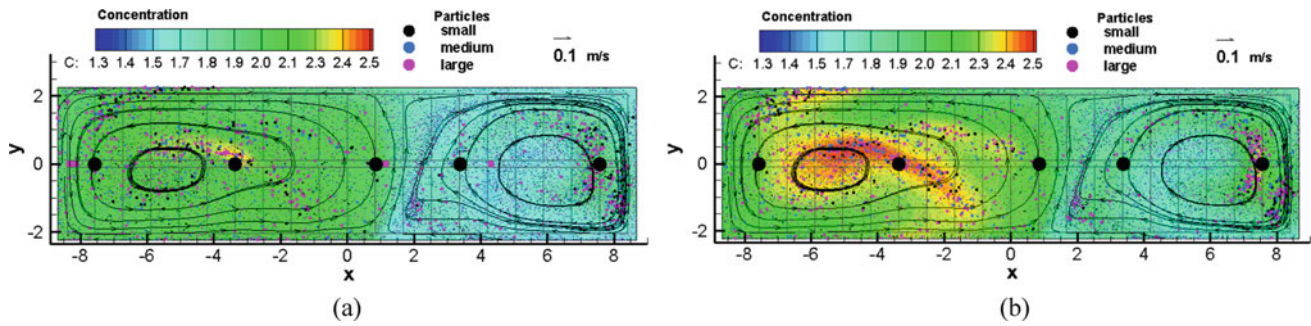
Fig. 9 Optimization of the feeder positions to give more uniform concentration after 1 h mixing: **a** accounting for the rafts, **b** no rafts
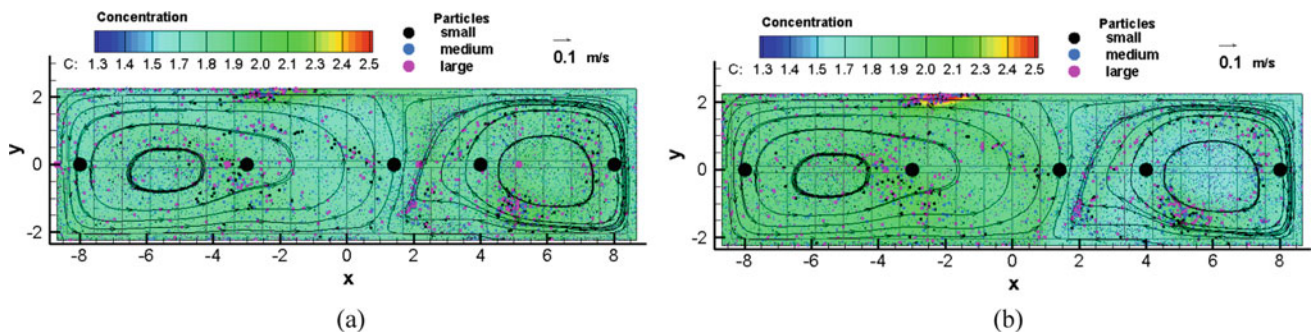

Fig. 10 Further optimization of the feeder positions to give more uniform concentration after 1 h mixing: **a** accounting for the rafts, **b** no rafts

resulting in the underfeed at the cell right-hand side and overfeed at the left-hand side, however retaining the global average concentration close to the initial and desired value of 2%. The concentration distribution can be improved either by supplying a variable alumina mass to the feeders (adding at the right side and reducing proportionally at the left side) or positioning the feeders in different locations. The latter is attempted in the simulation run presented in Fig. 9. The figure also compares the outcome for the raft model or the absence of the rafts (all particles are of the given small sizes): the rafts ensure more uniform dissolved material distribution because they act as additional 'feeder' positions while the rafts move and disperse gradually. An even further optimization by moving the feeders permits even better uniformity of the solution concentration while retaining the average close to 2% (Fig. 10).

Apparently, the velocity and the turbulent diffusivity distribution are crucial for the choice of the feeder positioning or loading if the uniformity of the feed concentration is required. Figure 11 demonstrates what happens if the cell is subject to some disturbance (for instance, by an anode change): there is a significant underfeed on the RHS of the cell with trapping of significant particle numbers in vortex centres of the perturbed flow. The LHS of the cell holds a

noticeable overfeed $\sim 2.5\%$ exceeding the average. This situation indicates a possibility to trigger anode effects due to the underfeed on the RHS of the cell. The further optimization by adding more feed mass through the feeder N5 (the last on RHS) at 2.5 kg, while all remaining are fed at 2.1 kg per cycle. The total feed amount remains the same as previously. The result is presented in Fig. 11b showing a better uniformity and the average retained close to the 2% level. This example shows that it is not enough to predict the total mass or average concentration. The local level of the dissolved alumina could be dropping dangerously low.

Conclusions and Future Work

The present work is a part of an on-going effort to develop a fast and efficient alumina dissolution model that could be used to optimize PBF locations and alumina feed uniformity. The paper presents the first attempt to incorporate the physics involving the raft presence, displacement, and dissolution in a full cell alumina feeding model. This attempt is an ongoing project; it is an incremental step in the development, however, it does not include the full physics of the raft dispersion in a way that the raft solid hull thickness
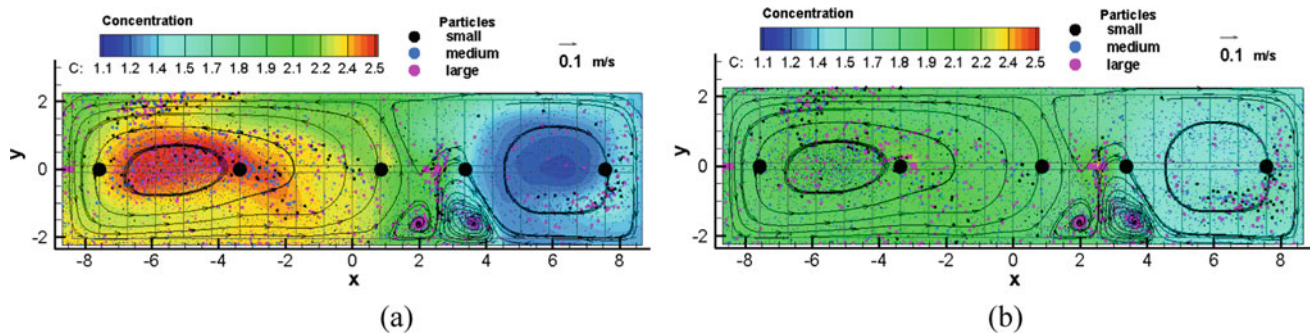
Fig. 11 a The perturbed velocity field: a failed feeder positioning gives highly nonuniform concentration after 1 h mixing (accounting for the rafts). **b** Further optimization of the individual feeder loads (add more mass at the feeder N5) gives more uniform concentration after 1 h mixing

gradually erodes to zero and the remaining fine particles are released at once at the new position where the raft ceases to exist. The present version does this gradually while the raft is still moving. Further user inputs could be added to allow the setup of feeding cycles by activating the feeders sequentially, not at once in each cycle; and a possibility to follow up long periods of underfeed, to be followed by overfeed period, as it is normally implemented in the industrial cells. Clearly, more work is needed, but the presented results indicate that the objective of developing a fast and efficient alumina dissolution model for design purposes is achieved.

References

1. Tabsh I, Dupuis M. and Gomes A. (1996) Process Simulation of Aluminum Reduction Cells, Light Metals 1996, TMS, 451–457.
2. Potocnik V. and Reverdy M. (2020) History of Computer Control of Aluminum Reduction Cells, Light Metals 2020, TMS, 591–597.
3. Wong D. S. and Marks J. (2013) Continuous PFC Emissions Measured on Individual 400 kA Cells", Light Metals 2013, TMS, 865–870.
4. Jassim A. and al. (2015) Studies on Background PFC Emission in Hall-Héroult Reduction Cells Using Online Anode Current Signals, Light Metals 2015, TMS, 545–550.
5. Dando N. R. and al. (2015) Non Anode Effect PFCS: Measurement Considerations and Potential Impacts, Light Metals 2015, TMS, 551–555.
6. Gylver S. E. and al. (2019) Alumina Feeding and Raft Formation: Raft Collection and Process Parameters, Light Metals 2019, TMS, 659–666.
7. Kaszas C. (2020) Behaviour of Alumina Power Fed into Molten Electrolytic Bath, PhD dissertation University of Québec at Chicoutimi.
8. Yang Y. and al. (2013) Mechanism of Dissolution Behavior of the Secondary Alumina, Metallurgical and Materials Transaction B, Vol 44B, Oct, 1296–1303.
9. Feng Y, Cooksey, M. A. and Schwarz, M. P. (2010) CFD Modeling of Alumina Mixing in Aluminium Reduction Cells", Light Metals 2010, TMS, 455–460.
10. von Kaenel R., Antille J., Romerio M.V., Besson O. (2013) Impact of magnetohydrodynamic and bubble driving forces on the alumina concentration in the bath of Hall-Héroult cell. In Sadler, B (ed) Light Metals 2013, TMS, 585–590.
11. Zhan S. and al. (2014) CFD simulation of dissolution process of Alumina in an Aluminum Reduction Cell with Two-Particle Phase Population Balance Model, Applied Thermal Engineering, 73, 805–818.
12. Bardet B, Foetisch T, Renaudier S, Rappaz J, Flueck M, Picasso M (2016) Alumina dissolution modelling in aluminium electrolysis cell considering MHD driven convection and thermal impact. In Williams, E. (ed) Light Metals 2016, TMS, 315–319.
13. Roger T. and al. (2021) Coupled SPH-DEM to Simulate the Injection of a Powder into a Liquid with Heat Transfer and Phase Change, Light Metals 2021, TMS, 368–376.
14. Bojarevics V. (2019) Dynamic modelling of alumina feeding in an aluminium electrolysis cell. In Chesonis C. (ed), Light Metals 2019, TMS, 675–682.
15. Bojarevics V. (2020) In-Line Cell Position and Anode Change Effects on the Alumina Dissolution. In L. Perander (ed.), Light Metals 2021, TMS, 584–590.
16. Lavoie P., Taylor M.P., Metson J. B. (2016) A Review of Alumina Feeding and Dissolution Factors in Aluminium Reduction Cells, Metall.Materials Trans. 47B: 2690– 2696.
17. Kovács A., Breward C.J.W., Einarsrud K.E., Halvorsen S.A., Nordgård-Hansen E., Manger E., Münch A., Oliver J.M., (2020) A heat and mass transfer problem for the dissolution of an alumina particle in a cryolite bath, International Journal of Heat and Mass Transfer, Volume 161, 120232.
18. Zhang H,Yang S, Zhang H, Li J, Xu Y (2014) Numerical simulation of alumina mixing process with a multicomponent flow model coupled with electromagnetic forces in aluminum reduction cells. JOM 66(7): 1210–1217.
19. Einarsrud K.E., Gylver S.E., Manger E. (2018) CFD modelling of alumina feeding. In Martin, O (ed) Light Metals 2018, TMS, 557–564.
20. Dagoberto S. Severo, Vanderlei Gusberti, Pablo Navarro and Marcos Domínguez (2018) Numerical Modeling of the Alumina Distribution in Aluar Cells, Travaux 47, Proceedings of the 36th International ICSOBA Conference, Belem, Brazil: 931–946.
21. Xiaozhen Liu, Youjian Yang, Zhaowen Wang, Wenju Tao, Tuofu Li, and Zhibin Zhao (2019) CFD Modeling of Alumina Diffusion and Distribution in Aluminum Smelting Cells, JOM 71(2): 764–771.
22. Kissane J.P. (1995) Optimising Alumina Feeders in Aluminium smelting pots, PhD Thesis, University of Wollongong, Australia.

23. Bojarevics V., Radionov E., Tretiyakov Y. (2018) Anode bottom burnout shape and velocity field investigation in a high amperage electrolysis cell. In Martin, O. (ed) Light Metals 2018. TMS, 551–556.

24. Bojarevics V., Pericleous K. (2009) Solutions for the Metal-Bath Interface in Aluminium Electrolysis Cells. In Light Metals 2009, TMS, 569–574.

25. Haverkamp RG, Welch BJ (1998) Modelling the dissolution of alumina powder in cryolite. Chem. Eng. Processing 37:177–187.

26. Wilcox D.C. (1998). Turbulence Modelling for CFD, 2nd ed., DCW Industries, California.

27. Rastogi A.K., Rodi W. (1978) Prediction of heat and mass transfer in open channels. J. Hydraulics Division ASCE, HY3: 397–420.

28. Tucker PG (2001) Computation of particle and scalar transport for complex geometry turbulent flows. Journ. Fluids Eng. 123:372–381.

29. Clift R, Grace JR, Weber ME (2005) Bubbles, Drops, and Particles. Dover Publications, New York.

30. Zhang L., Wang Sh., Dong A., Gao J., Damoah L.N.W. (2014) Application of Electromagnetic Separation Technology to Metal Refining Processes: Review, Metall. Materials Trans. 45B: 2153–2185.

31. Bojarevics V., Dupuis M. (2021) Application and Adaptability of MHD Stability Computation for Modern Aluminium Reduction Cells at Extreme Conditions of Low ACD. L. Perander (ed.), Light Metals 2021, The Minerals, Metals & Materials Series, 565–571.